



HAL
open science

The electrochemical performance of Ta₂O₅ thin films in ionic liquid and ionogel electrolytes

Patrick Gerlach, Cédric Teyssédou, Jérémie Chaillou, Isabelle Roch-Jeune, Camille Douard, Pascal Roussel, Jean Le Bideau, Christophe Lethien, Thierry Brousse

► To cite this version:

Patrick Gerlach, Cédric Teyssédou, Jérémie Chaillou, Isabelle Roch-Jeune, Camille Douard, et al.. The electrochemical performance of Ta₂O₅ thin films in ionic liquid and ionogel electrolytes. *Electrochimica Acta*, 2025, 514, pp.145568. 10.1016/j.electacta.2024.145568 . hal-04903955

HAL Id: hal-04903955

<https://nantes-universite.hal.science/hal-04903955v1>

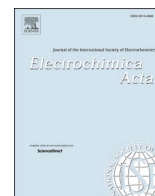
Submitted on 21 Jan 2025

HAL is a multi-disciplinary open access archive for the deposit and dissemination of scientific research documents, whether they are published or not. The documents may come from teaching and research institutions in France or abroad, or from public or private research centers.


L'archive ouverte pluridisciplinaire **HAL**, est destinée au dépôt et à la diffusion de documents scientifiques de niveau recherche, publiés ou non, émanant des établissements d'enseignement et de recherche français ou étrangers, des laboratoires publics ou privés.



Distributed under a Creative Commons Attribution 4.0 International License



The electrochemical performance of Ta₂O₅ thin films in ionic liquid and ionogel electrolytes

Patrick Gerlach^{a,b,1}, Cédric Teyssédou^{b,c,d}, Jérémie Chaillou^{c,d}, Isabelle Roch-Jeune^{b,c},
Camille Douard^{a,b}, Pascal Roussel^{d,2}, Jean Le Bideau^{a,b}, Christophe Lethien^{b,c,e,*},
Thierry Brousse^{a,b,*} 

^a Nantes Université, CNRS, Institut des Matériaux de Nantes Jean Rouxel, IMN, 2 rue de la Houssinière BP32229, CEDEX 3, Nantes F-44322, France

^b Réseau sur le Stockage Electrochimique de l'Energie (RS2E), CNRS FR 3459, 33 rue Saint Leu, CEDEX, Amiens F-80039, France

^c Institut d'Electronique de Microélectronique et de Nanotechnologies, Université de Lille, CNRS, Université Polytechnique Hauts-de-France, UMR 8520 – IEMN, Lille F-59000, France

^d Unité de Catalyse et de Chimie du Solide (UCCS), Université de Lille, CNRS, Centrale Lille, Université d'Artois, UMR 8181 – UCCS, Lille F-59000, France

^e Institut Universitaire de France (IUF) Saint-Michel 103, Paris 75005, France

ARTICLE INFO

Keywords:

High-power-energy storage

Hybrid micro-capacitor

Thin films

Ta₂O₅

MnO₂

Ionic liquids

Ionogel

ABSTRACT

In this work, we present a new cell design for miniaturized energy storage devices by realizing a hybrid micro-capacitor, which uses for the first time a TaN/ Ta₂O₅ thin film electrode in combination with a MnO₂ composite electrode. In this proof of concept study, the electrochemical performance of the dielectric material Ta₂O₅ was of main interest. Therefore, various tantalum oxide films with different thicknesses from 23 to 80 nm have been tested in combination with a pseudocapacitive oversized MnO₂ composite electrode. This was done with two model electrolytes, namely the ionic liquid Emim FSI and the solid-state ionogel Emim FSI: PVdF 80:20. Surface capacitance values up to 1.94 μF cm⁻² in Emim FSI and 2.84 μF cm⁻² in IG Emim TFSI: PVdF 80:20 have been reached at high scan rates (100 mV s⁻¹) with no significant distortion of the voltammograms. When films of 47 and 80 nm thickness of Ta₂O₅ are used, stable cycling with scan rates of up to 5000 mV s⁻¹ at a cell voltage of 20 V can be achieved even in solid-state ionogel electrolyte. This performance highlights the promising characteristics of these materials and cell concept for miniaturized high power energy storage application and opens the way for further investigations to improve this needed technology.

1. Introduction

Applications like *in-vivo* healthcare, smart packaging or smart wearables use miniaturized electronic devices such as sensors or micro motors. To power these devices, likewise miniaturized energy storage solutions are needed [1–3].

To do so, either micro-batteries (MBs) and or micro-capacitors (MCs) can be used to deliver the needed energy. The energy storage mechanism in these two devices differs significantly.

On the one hand, MBs exploit redox reactions of e.g. metal-ion based (Li, Na or Zn) faradaic thin films for the energy storage/ delivery, which provides high energy density [4–6]. MCs on the other hand are divided

in two main categories. In micro-dielectric-capacitors (MDC) an dielectric material is polarized in the electric field between two metal electrodes [7] (Fig. 1A). Since this polarization is an exclusively physical process with no mass transport or present electrolyte to encounter parasitic reactions, very high cell voltage, power and lifetime can be achieved [7].

The capacitance (and therewith the energy density) of these devices depends on the substrate area *A*, the relative permittivity of the dielectric ϵ_r and the thickness of the dielectric *l* and can be calculated via Eq. (1)

* Corresponding authors at: Réseau sur le Stockage Electrochimique de l'Energie (RS2E), CNRS FR 3459, 33 rue Saint Leu, CEDEX, Amiens F-80039, France.

E-mail addresses: Christophe.lethien@univ-lille.fr (C. Lethien), thierry.brousse@univ-nantes.fr (T. Brousse).

¹ Patrick Gerlach orcid id: 0009-0006-1230-7378.

² Pascal Roussel orcid id: 0000-0001-7243-7293.

³ Christophe Lethien orcid id: 0000-0001-8906-8308.

$$C = \epsilon_r \epsilon_0 \frac{A}{l} \quad (1)$$

where ϵ_0 is the permittivity of the vacuum ($\epsilon_0 = 8.85 \times 10^{-12} \text{ F m}^{-1}$) [8].

Another approach for MCs are micro-supercapacitors MSCs, which aims to increase the capacitance by increase of the surface area [9]. This includes electrochemical double layer capacitors (EDLCs) and pseudocapacitors [9].

In EDLCs, energy is stored via charge separation of ions in the electrolyte and the subsequent accumulation of ions on both opposite electrodes in a double layer (Fig. 1B). There, the electrolyte also works as electronic insulator but this process involves mass transport of charge carriers. Activated carbons are by far the most used capacitive electrode materials for EDLCs, but other carbons like carbide derived carbon are studied as well [10,11].

Pseudocapacitive materials, on the other hand, resemble the electrochemical I-V signature of pure capacitive electrode materials via the exertion of fast redox reactions on the surface of the electrodes over the used voltage range [12]. Transition metal oxides like RuO_2 , Nb_2O_5 or MnO_2 are common active materials for pseudocapacitors [13]. Typically, pseudocapacitors display higher capacitance/ energy density than EDLCs but are inferior to them in power performance [14].

In this work, we present for the first time a new concept for MCs where we combine a dielectric material electrode on one side of the MC with a pseudocapacitive electrode on the other side. Based on recent paper on electrolytic micro-capacitor published recently [15] where dielectric electrode is combined with metal electrode in aqueous electrolyte, we extend this concept towards hybrid micro-capacitor technologies combining dielectric and pseudocapacitive electrodes in solid-state configuration. An electrolyte separates them, realizing a micro hybrid capacitor (MHC). This novel hybrid design represents an innovative energy storage concept since in the device, energy is stored via charge separation in the dielectric electrode and the electrolyte, which results in the utilization of two charge separation media present in the cell instead of the usual one (Fig. 1C). At the same time during charge, energy is stored at the pseudo capacitive electrode by redox reactions and ion adsorption at the electrode surface (Fig. 1C). With this approach, we aim to fuse high cell voltage and high energy density for a device performing in the energy and power area in between supercapacitors and MCs (Fig. 2). Specifically, the final cell design implements a Ta_2O_5 thin film as positive electrode, an ionic liquid (IL) or ionogel (IG) as the electrolyte and MnO_2 as negative electrode active material (Fig. 1D).

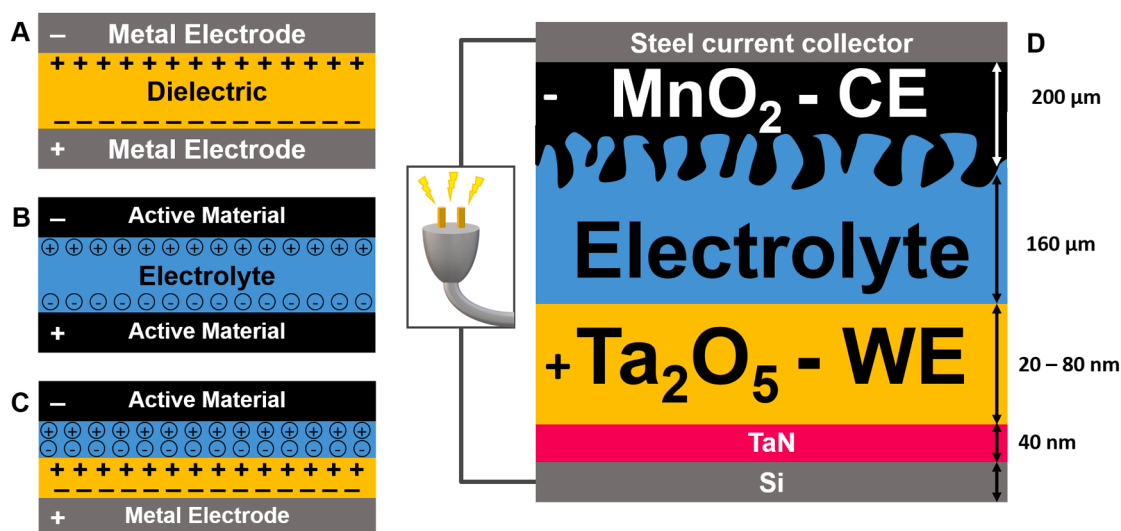


Fig. 1. Simplified schematic representation of (A) a charged micro dielectric capacitor, (B) a charged electrochemical double layer capacitor, (C) our new approach of the combination of a dielectric positive electrode and a double layer negative electrode and (D) detailed depiction of the realized micro hybrid device.

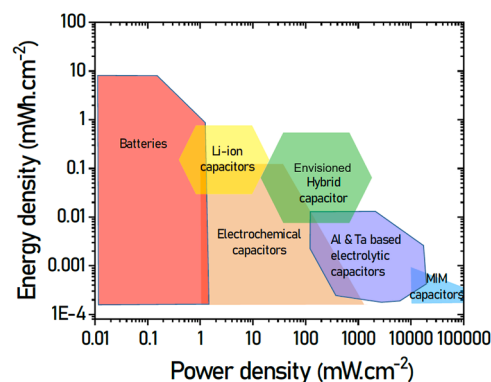


Fig. 2. Ragone plot of different energy storage devices.

Ta_2O_5 is known for its high dielectric constant of 25, its good dielectric breakdown strength of 0.5 V nm^{-1} [16,17] and its high chemical stability [18]. Thanks to these features, Ta_2O_5 is used since decades as dielectric barrier layer in tantalum electrolytic capacitor for energy storage application [19].

MnO_2 is a commonly used pseudocapacitor material due to its abundance and low cost [20,21]. Symmetrical systems using MnO_2 report values of 25 F g^{-1} at a scan rate of 10 mV s^{-1} [22].

Furthermore, it was investigated for thin film energy storage [23–25]. A symmetrical 1 V micro supercapacitor using MnO_2 electrodes in Emim TFSI ionogel, for example, delivered 25 mF cm^{-2} even at elevated scan rates of 100 mV s^{-1} [26].

Unlike metal-dielectric-metal capacitors, the here presented cell design is in need of an electrolyte for the MnO_2 electrode. Specifically, cations of the electrolyte are needed for compensation of charges during the reduction of MnO_2 in the charging process as shown in Eq. (2) [23].



To test the described system two electrolytes have been chosen, namely the ionic liquid (IL) 1-ethyl-3-methylimidazolium bis(fluorosulfonyl)imide (Emim FSI) and the corresponding ionogel (IG) Emim FSI: PVdF 80:20.

Ionic liquids are salts with low lattice energies and, therewith, low melting points below $100 \text{ }^\circ\text{C}$ [27]. In the case of Emim FSI, the melting point is even found at $-14 \text{ }^\circ\text{C}$ [28]. This makes it usable as a room temperature electrolyte, where it has been used successfully as

electrolyte for SCs and batteries [27,29].

Furthermore, to realize an all-solid-state approach for the presented MHC, we decided to confine Emim FSI in a polymer matrix of poly vinylidene fluoride (PVdF) in the weight ratio of 80 % ionic liquid and 20 % polymer. Therewith, a quasi-solid ionogel electrolyte is created, which retains many of the initial properties of the confined ionic liquid like low vapor pressure, non-flammability, feasible conductivity, large electrochemical stability window and wide thermal range [27,30,31]. Next to other applications, IGs were intensively studied for electrochemical storage applications [32–34]. In a recent work, our research group proved the usability of IGs in combination with symmetrical MnO₂ thin film cell designs [26]. However, to the best of our knowledge no studies using Ta₂O₅ thin films have been reported.

The electrochemical performance of the realized MHC is discussed below in the section results and discussion.

2. Results and discussion

At first, the characterization of various thin films made by magnetron sputtering deposition techniques has been performed. Two layers (TaN/Ta₂O₅) were stacked on a Si wafer to form the dielectric electrode. Each layer was carefully analyzed. A 100 nm thick TaN layer deposited by magnetron sputtering deposited on a [001] oriented-Si substrate was characterized by XRD analysis and Raman spectroscopy. The diffractograms of TaN film is shown in Fig. 3A. We can notice two Bragg peaks located at $2\theta = 34.50^\circ$ and 41.16° . The first peak, asymmetric, can be assigned to the (110) peak of the hexagonal TaN (JCPDS 00–039–1485) as well as the (111) peak of the cubic TaN (JCPDS 00–049–1283). The second peak at $2\theta = 41.16^\circ$ can be attributed to the (200) peaks of the cubic TaN. The XRD analysis shows that the TaN layer is actually composed of two phases. Raman analyses were also carried out. The spectrum is shown in Fig. 3B. Two Raman peaks located at $118\text{ cm}^{-1} \pm 5\text{ cm}^{-1}$ and $189\text{ cm}^{-1} \pm 10\text{ cm}^{-1}$ can be attributed respectively to Ta-N bond first-order transversal acoustic mode and first-order longitudinal acoustic mode [35].

The chemical composition of the tantalum oxide layer (100 nm-thick) was analyzed by XPS. The Fig. 4 shows the Ta 4f core level spectra and its deconvolution. After deconvolution, only one contribution allows for a correct fit of the experimental spectrum. The binding energy of the Ta 4f_{7/2} core level is located at 27.1 eV, which corresponds to the signature of Ta₂O₅ as reported in the literature meaning that the obtained layer corresponds well to the desired stoichiometry (Ta₂O₅) [36]. XRD analysis (not shown here) clearly confirm the amorphous nature of the Ta₂O₅ film as expected for a dielectric electrode in micro-capacitor or hybrid micro-device.

In this work the thickness effect of several sputtered Si / TaN / Ta₂O₅ electrodes were investigated. Specifically, Ta₂O₅ dielectric layer

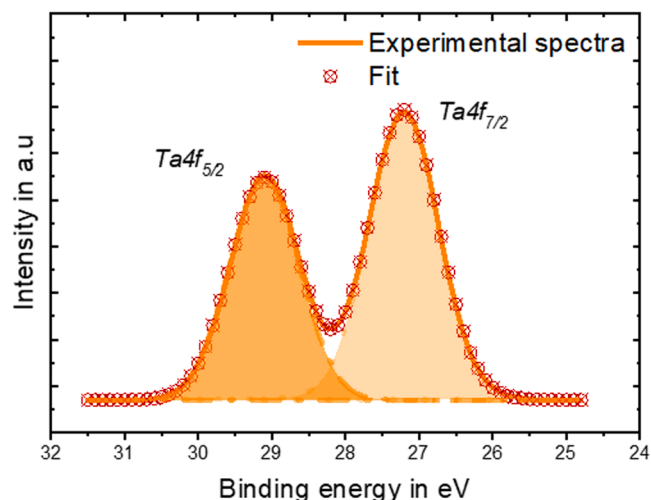


Fig. 4. XPS analyses of a Ta₂O₅ magnetron sputtering layer 100 nm thick deposited on [001] oriented-Si substrate at the Ta 4f core level.

thickness was varied (~ 20, 40, and 80 nm) while the thickness of TaN film was kept constant at ~ 40 nm. Fig. 5A shows cross-sectional SEM images of the three tested electrodes. The thicknesses were confirmed by SEM cross sections images. We also observe that the Ta₂O₅ microstructure is compact in good agreement with what is sought for barrier dielectric layers.

As the SEM resolution is too low to accurately determine the Ta₂O₅ thicknesses when nanometer-thick films are currently investigated, we performed further analyses by X-Ray Reflectivity (XRR). This characterization technique allows accessing to nanometer range thickness resolution by analyzing the oscillation interferences period, which is inversely proportional to the thickness of a layer [37]. The XRR measurements and the fitting results of the ~ 40 / 20 and ~ 40 / 40 nm-thick TaN / Ta₂O₅ electrodes are depicted in Fig. 5B and C. XRR analyses confirm two different oscillations periods range, meaning that the TaN and the Ta₂O₅ layers have different thicknesses. After fitting processes, made with Reflex software [38], the TaN layer is refined at 43 nm-thick and the Ta₂O₅ at 23 nm-thick. For Fig. 5C the process fitting converges to a TaN thickness of 45 nm and a Ta₂O₅ one of 47 nm. For the Ta₂O₅ layer, the bulk density was also evaluated to 7.9 g.cm⁻³ (theoretical bulk density = 8.2 g.cm⁻³) in good agreement with the observed compact microstructure of the stacked layers observed in Fig. 5A.

Fig. 6 displays the ionic conductivity of pure Emim FSI and confined Emim FSI in PVdF IG 80:20 in the temperature range of –20 to 80 °C. The points of most interest are measured at 20 °C at which the electrochemical performance tests have been carried out. As expected, the

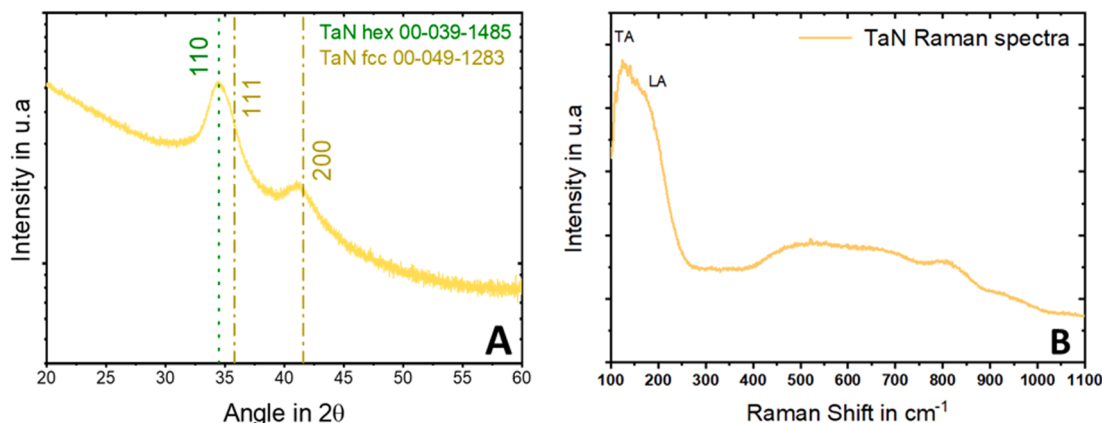


Fig. 3. Structural analyses of the 100 nm-thick sputtered TaN films. (A) XRD analyses, (B) Raman spectroscopy measurement.

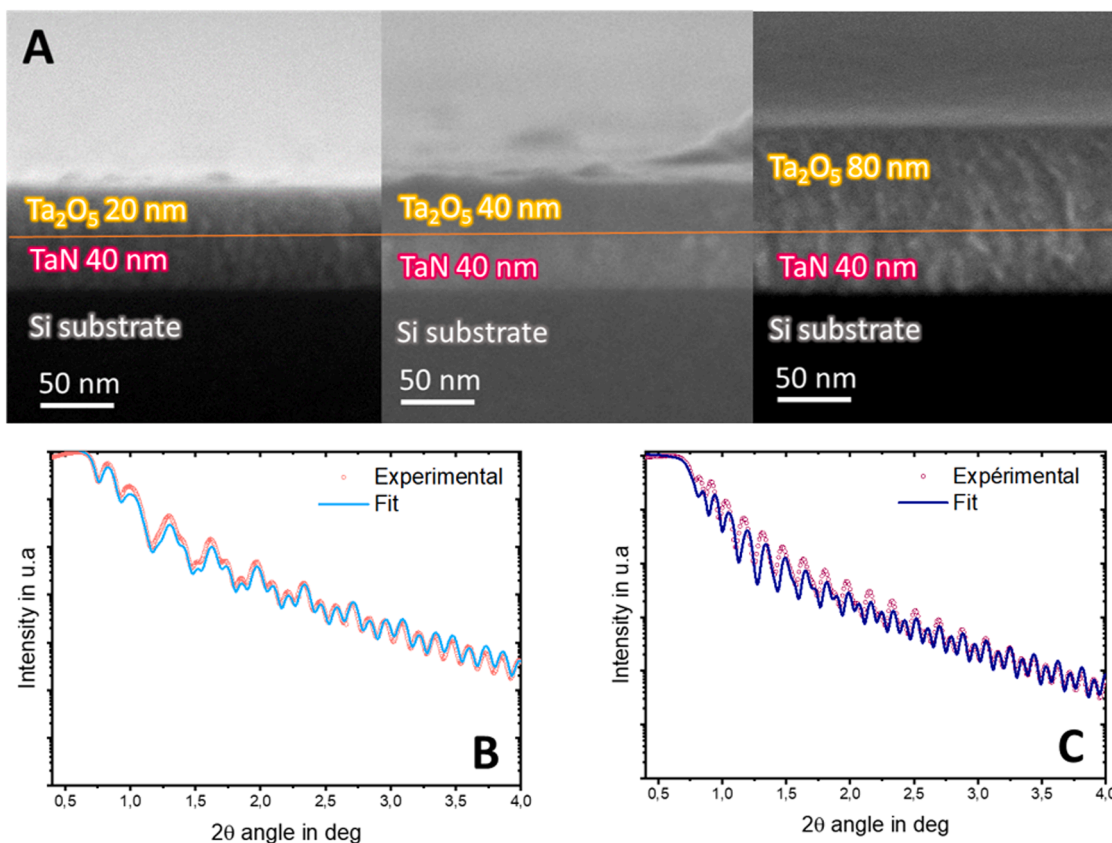


Fig. 5. Analyses of the TaN/Ta₂O₅ electrode deposited by magnetron sputtering on [001] oriented-Si substrate. (A) SEM cross section images of the three TaN/Ta₂O₅ electrodes. (B) XRR analyses of the TaN/Ta₂O₅ refined to a 43/23 nm thick electrode. (C) XRR analyses of the TaN/Ta₂O₅ 45/47 nm thick electrode.

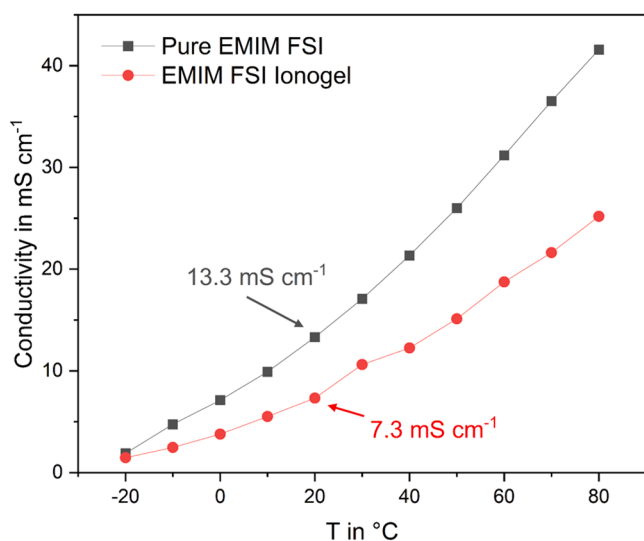


Fig. 6. Conductivity of pure Emim FSI and Emim FSI in PVDF Ionogel 80:20 at -20 to 80 °C.

pure liquid Emim FSI displays a higher conductivity of 13.3 mS cm^{-1} . However, with a value of 7.3 mS cm^{-1} , the IG is well usable as electrolyte for the electrochemical investigations of this study and comparable with other investigated electrolytes for high power energy storage applications [39].

Fig. 7 presents the first electrochemical measurements of the used Ta₂O₅ thin films with thicknesses of 23, 47 and 80 nm in the above-described full-cell setup in combination with an oversized MnO₂

counter electrode. At first, cyclic voltammograms (CVs) have been carried out for different cell voltages ranging from 1 to 20 V at a scan rate of 100 mV s^{-1}

The left column represents the results obtained in Emim FSI (Fig. 6A, C and E) while the right column displays the cycles in the IG Emim FSI: PVDF for the different thicknesses (Fig. 6B, D and F).

The term cell voltage is used here, since there is no reference electrode present in the described cell setup and the term potential is therefore inaccurate. Nevertheless, since a largely oversized counter is applied, the reported values of current and voltage correspond nearly exclusively to the electrochemical behavior of the used Ta₂O₅ thin films.

For the thicknesses of 23 nm of Ta₂O₅, a similar behavior is visible in both Emim FSI as well as Emim FSI: PVDF (Fig. 7A and B). Until the cell voltage of 10 V, the 23 nm films are cycling with a rectangular shape with an aerial capacitance value of $1.94 \mu\text{F cm}^{-2}$ in Emim FSI and $2.84 \mu\text{F cm}^{-2}$ in Emim FSI: PVDF, which represents the capacitive behavior of the Ta₂O₅ dielectric. In both electrolytes at 15 and 20 V, parasitic irreversible currents are obtained, which marks the dielectric breakdown of the Ta₂O₅ films. This means that the applied current exceeds the capability of the film to resist the applied voltage. This forces the material to conduct current again, which is then causing degradation of the electrolyte as seen. The theoretic breakdown field of Ta₂O₅ is $5 \times 10^6 \text{ V cm}^{-1}$ [16,40,41]. For the used film thickness of 23 nm, this value results do a specific breakdown voltage of

$$V_{Break} = V_{th} \times d_{film} \quad (3)$$

$$V_{Break} = 5 \times 10^6 \text{ V cm}^{-1} \times 23 \times 10^{-7} \text{ cm} = 11.5 \text{ V}$$

which explains why we observe parasitic reactions of the electrolyte once we exceed this voltage. For the higher film thickness of 47 nm, this breakdown does not occur (Fig. 7C and D) with the exception of a slight

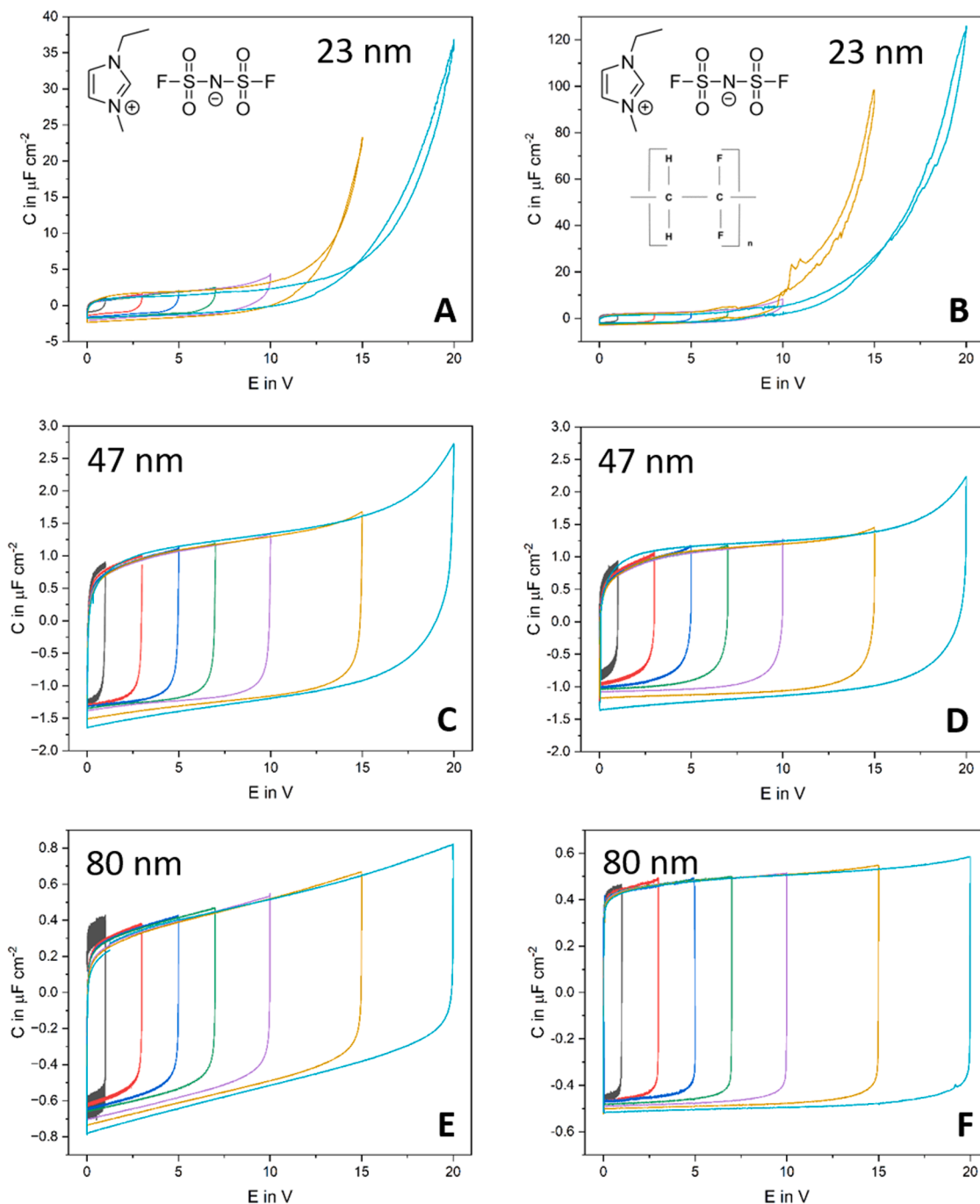


Fig. 7. Cyclic voltammograms at 100 mV s^{-1} with cell voltages ranging from 1 to 20 V for (A) and (B) Ta_2O_5 film thickness of 23 nm, (C) and (D) Ta_2O_5 film thickness of 47 nm, (E) and (F) Ta_2O_5 film thickness of 80 nm in pure Emim FSI and Emim FSI in PVdF Ionogel 80:20.

diversion from the rectangular shape at high voltages around 20 V. For both electrolytes, capacitances of $1.35 \mu\text{F cm}^{-2}$ (Emim FSI) and $1.25 \mu\text{F cm}^{-2}$ (Emim FSI: PVdF) are obtained.

For 80 nm of Ta_2O_5 (Fig. 7E and F), a more resistive behavior is shown in pure Emim FSI, which results to a hysteresis for all CVs. In the IG, however, a perfect rectangular shape is measured at all cell voltages up to 20 V with a capacitance of $0.51 \mu\text{F cm}^{-2}$. At this point, it is noteworthy to highlight that the increase in Ta_2O_5 film thickness results to a decrease in areal capacitance, which is in line with Eq. (1), since the separated charges are more distant from another.

Based on these results, out of the three investigated films, the Ta_2O_5 film with a thickness of 47 nm is most promising for devices operating at high voltage with feasible areal capacitance.

Fig. 8 compares the rate capability performance of Ta_2O_5 thin films at scan rates from 100 to 5000 mV s^{-1} with a cell voltage of 20 V in IL and IG electrolyte.

For lower scan rates of especially 100 and 200 mV s^{-1} the same phenomenon of parasitic currents is visible at high cell voltages in Fig. 8A and B as it was presented already in Fig. 7A and B. With the application of higher scan rates, beginning from 1000 mV s^{-1} , the intensity of these parasitic currents is decreasing as scanning speeds surpass the kinetics of unwanted reactions. At 5000 mV s^{-1} perfect rectangular CVs are obtained. Similar but less pronounced phenomena are observed for 47 nm in Fig. 8C and D. While at 100 and 200 mV s^{-1} the indication of peak currents are visible at 20 V, none of the like is seen beginning from 500 mV s^{-1} . Furthermore, at 5000 mV s^{-1} distortion from

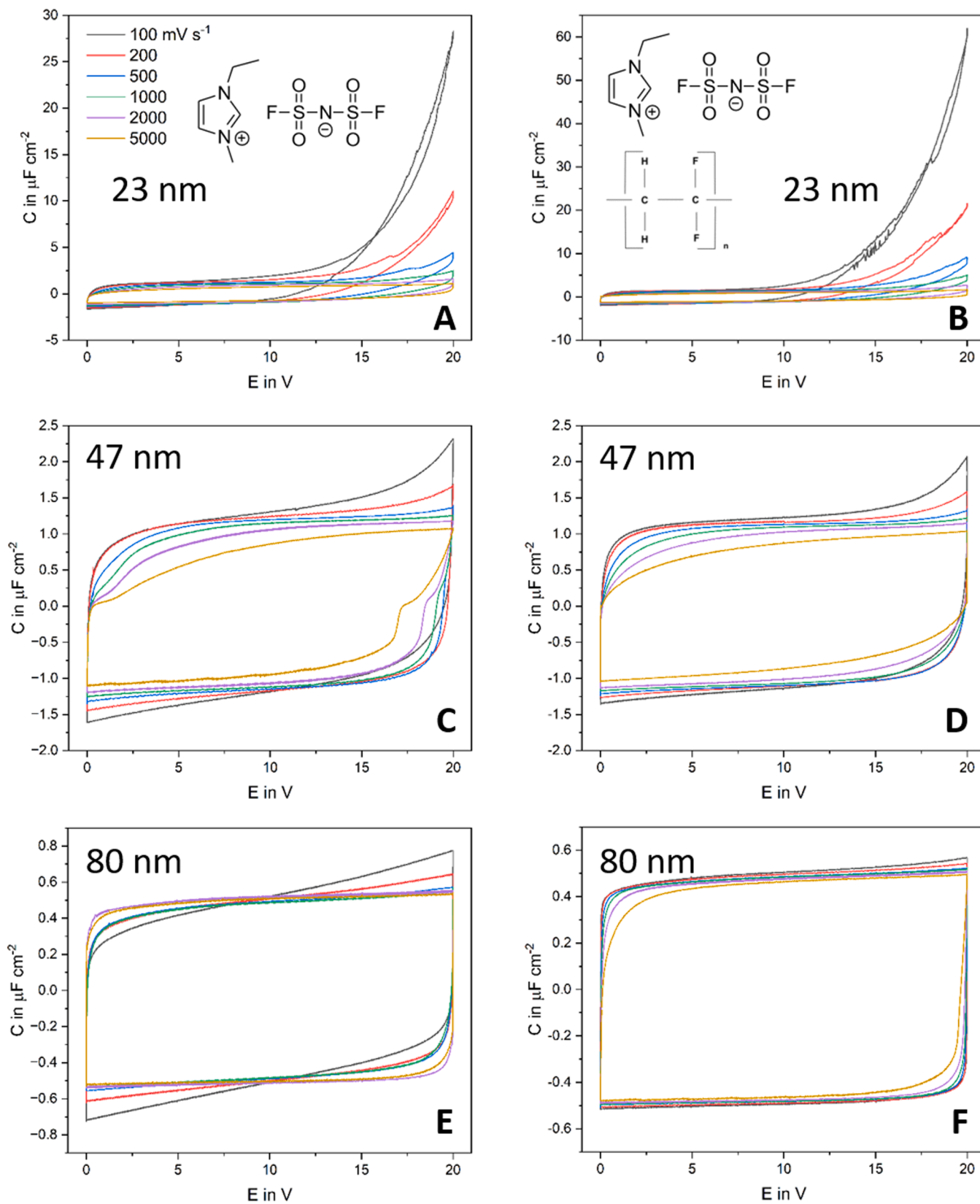


Fig. 8. Cyclic voltammograms at 100 to 5000 mV s^{-1} with a cell voltage of 20 V for (A) and (B) Ta_2O_5 film thickness of 23 nm, (C) and (D) Ta_2O_5 film thickness of 47 nm, (E) and (F) Ta_2O_5 film thickness of 80 nm in pure Emim FSI and Emim FSI in PVdF Ionogel 80:20.

the pure capacitive shape is found for CVs in Emim FSI. The same cannot be found in the IG.

With the 80 nm films (Fig. 8E and F) no irreversible peaks are measured even at 100 mV s^{-1} and very rectangular CV are found for all scan rates.

For a better comparison of the capacitances in the rate experiments, the absolute and relative values of the capacitances with respect to the scan rate (each taken at cell voltage of 10 V) are displayed in Fig. 9.

Fig. 9A and B compare the evolution of absolute capacitance values for all Ta_2O_5 thicknesses in combination with IL and IG. For both electrolytes, the highest capacitance value is obtained for 23 nm at 100 mV s^{-1} with 1.93 for the IL and $2.55 \mu\text{F cm}^{-2}$ for the IG, respectively. Both curves for 23 nm decay rapidly with increasing scan rates. At 5000 mV s^{-1} , $0.62 \mu\text{F cm}^{-2}$ are measured for Emim FSI while $0.84 \mu\text{F cm}^{-2}$ are obtained in combination with the IG Emim FSI: PVdF. For 47 nm of Ta_2O_5 , a much more linear decay of the capacitance can be seen. For the IL, at 100 mV s^{-1} $1.3 \mu\text{F cm}^{-2}$ are presented, which reduces to $0.69 \mu\text{F cm}^{-2}$. For the IG, similar values are achieved; $1.2 \mu\text{F cm}^{-2}$ at 100 mV s^{-1} and $0.78 \mu\text{F cm}^{-2}$, respectively.

The films of 80 nm display very stable capacitances in both electrolytes nearly independent from the applied scan rate. The IL displays $0.52 \mu\text{F cm}^{-2}$ at 100 mV s^{-1} , which reduces to $0.49 \mu\text{F cm}^{-2}$ at 5000 mV s^{-1} . The IG on the other hand, shows $0.51 \mu\text{F cm}^{-2}$ at 100 mV s^{-1} and $0.45 \mu\text{F cm}^{-2}$ at 5000 mV s^{-1} . In absolute values, the lowest capacitances of all tested film thicknesses are measured here.

The described evolutions are also presented in Fig. 9C and D in relative values where the obtained values at 100 mV s^{-1} were set to 100 % for all combinations of film thickness and electrolytes. While at 80 nm a capacitance retention of 94.5 % and 88.2 % were realized for the two

electrolytes at 5000 mV s^{-1} , at 23 nm, only 33 % are possible for both electrolytes. 47 nm displays a performance between the two. For the IL, 53 % at 5000 mV s^{-1} can be retained. For the IG, even 65 % at 5000 mV s^{-1} are possible.

Therewith the highest capacity retention with reasonable values of absolute capacitance is measured for 47 nm Ta_2O_5 with the IG.

The last electrochemical consideration performed in this study concerns the cycling stability of the tested films in Fig. 10.

Fig. 10A and B compare the cycling stability of 23 nm films of Ta_2O_5 in Emim FSI and Emim FSI: PVdF electrolyte during 200 cycles of CVs at 500 mV s^{-1} . Both graphs display a similar behavior. During the first cycle, irreversible oxidation currents are obtained at voltages higher than 15 V. With continuous cycling, these currents decline, as probably less and less species to oxidize are present next to the electrode surface. The capacitances measured at 10 V in Fig. 10A reduced from $1.33 \mu\text{F cm}^{-2}$ to $1.01 \mu\text{F cm}^{-2}$ over the course of 2000 cycles, which represents a capacitance loss of 24 %. In Fig. 10B, $1.58 \mu\text{F cm}^{-2}$ are measured for the first cycle, while $1.57 \mu\text{F cm}^{-2}$ are seen at cycle 2000. Although this marks a retention of 99 %, the unsteady cycling displayed in the graph indicate a very unstable cycling.

As seen before, much less parasitic reactions are present for the 47 nm films. Minor peaks are seen at 20 V using the IL in Fig. 10C, while in the IG, they are still observed during cycle 100 in Fig. 10D. In the IL, $1.3 \mu\text{F cm}^{-2}$ are measured for the first cycle, which reduces to $1.2 \mu\text{F cm}^{-2}$ after 2000 cycles. In the IG, values of $1.2 \mu\text{F cm}^{-2}$ for the first cycle and $1.1 \mu\text{F cm}^{-2}$ for the 2000th cycle are measured. With these results, similar capacity retentions of 92.3 % and 91.7 % are calculated for the IL and IG.

In Fig. 10E and F, most rectangular shapes for the CVs with highest

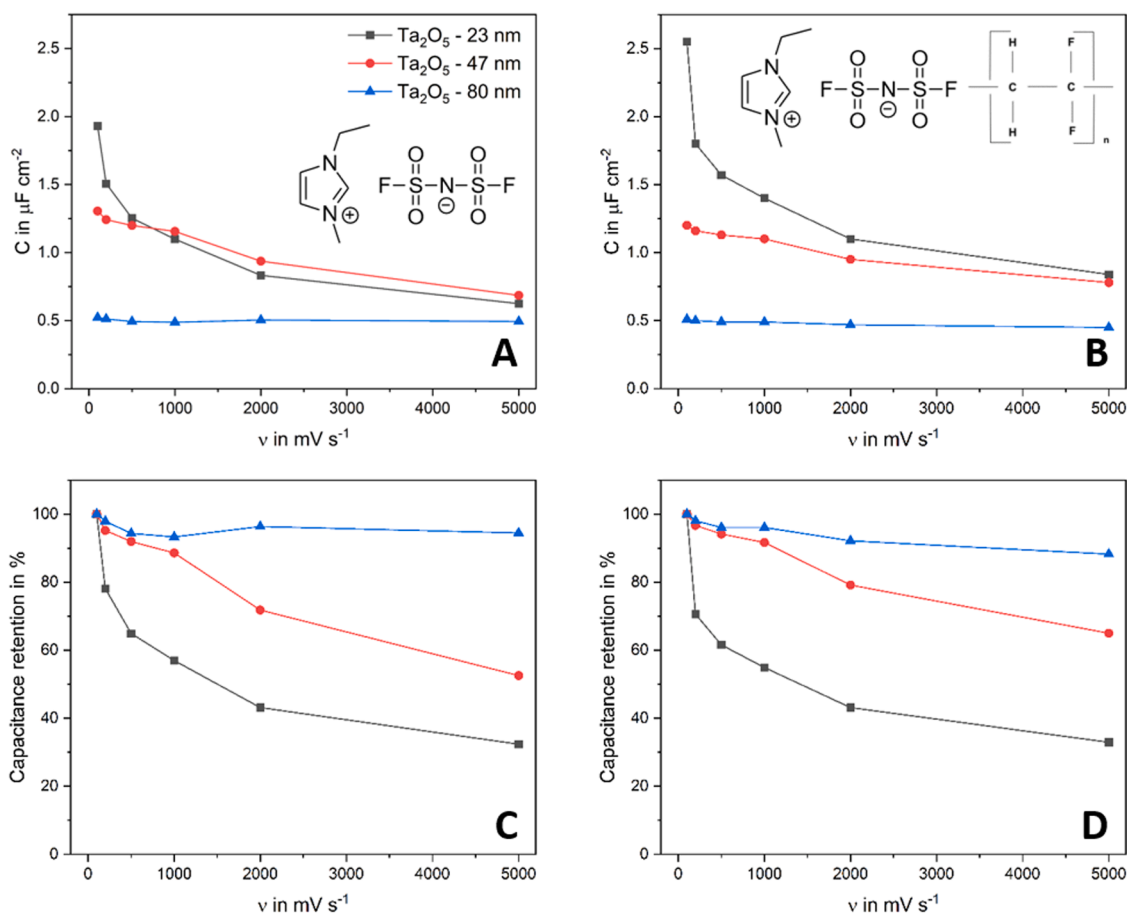


Fig. 9. Rate capability comparison for scan rates ranging from 100 to 5000 mV s^{-1} with a cell voltage of 20 V for (A) and (B) Ta_2O_5 film thickness of 23 nm, (C) and (D) Ta_2O_5 film thickness of 47 nm, (E) and (F) Ta_2O_5 film thickness of 80 nm in pure Emim FSI and Emim FSI in PVdF Ionogel 80:20.

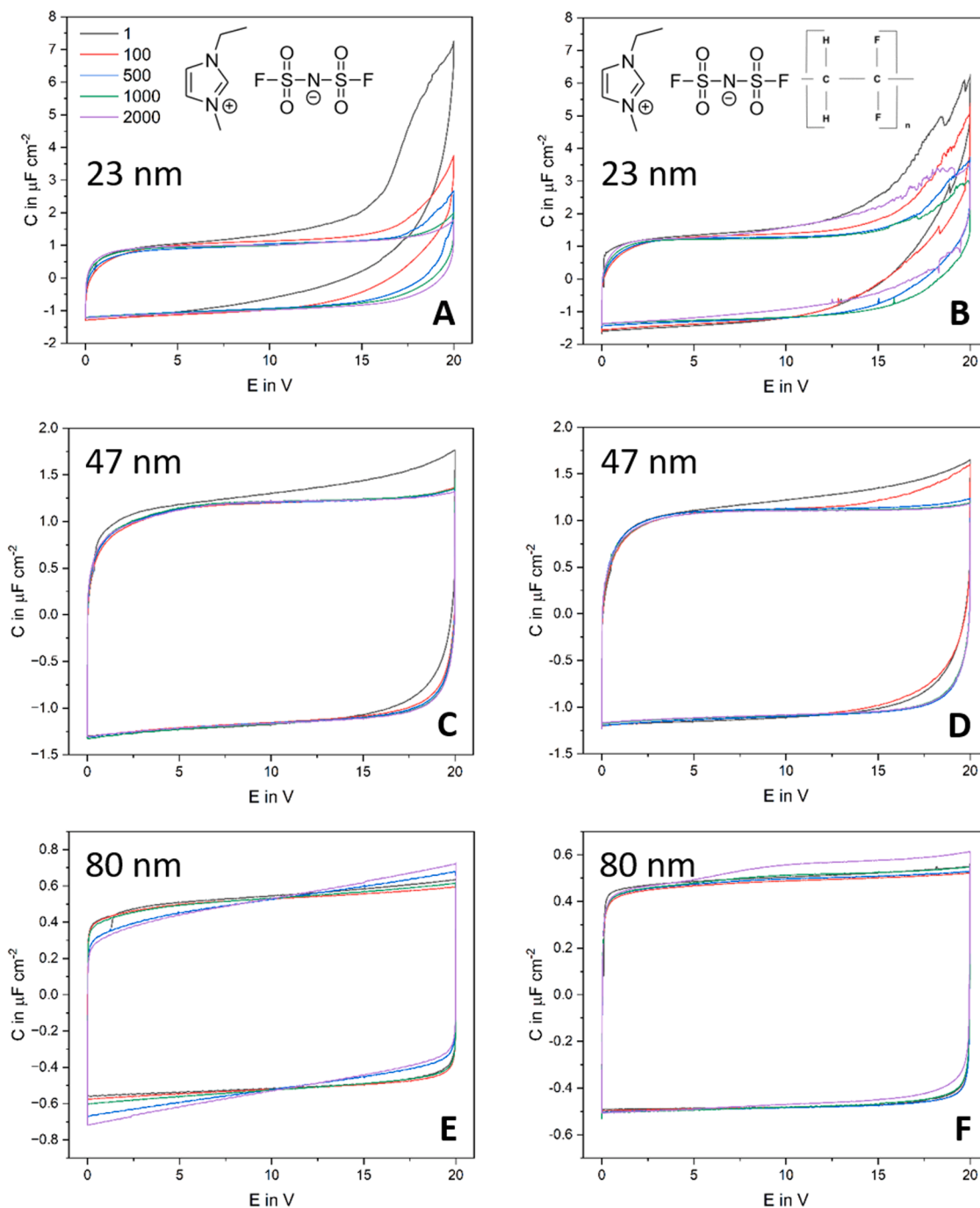


Fig. 10. 2000 cycles of cyclic voltammograms at 500 mV s^{-1} with a cell voltage of 20 V for (A) and (B) Ta_2O_5 film thickness of 23 nm, (C) and (D) Ta_2O_5 film thickness of 47 nm, (E) and (F) Ta_2O_5 film thickness of 80 nm in pure Emim FSI and Emim FSI in PVdF Ionogel 80:20.

capacitance retentions among the three thin film thicknesses are reported. For Emim FSI in combination with 80 nm of Ta_2O_5 , the capacitances evolve from $0.55 \mu\text{F cm}^{-2}$ to $0.53 \mu\text{F cm}^{-2}$ with a retention of 96.4 %. At the same time, capacitances of $0.51 \mu\text{F cm}^{-2}$ and $0.56 \mu\text{F cm}^{-2}$ are achieved, which displays an improvement in capacitance of 10 %.

Based on these results 80 nm of Ta_2O_5 in the IG display the highest cycling stability among the tested combinations.

3. Conclusion

In this work, we successfully presented a proof of concept for a MHC using Ta_2O_5 dielectric thin film electrodes in combination with oversized MnO_2 composite electrodes and ionic liquid Emim TFSI or IG

Emim TFSI: PVdF 80:20 electrolyte. To do so, 40 nm-thick TaN current collector was deposited by reactive sputtering deposition method on Silicon wafer. Ta_2O_5 thin films have been sputtered with various thicknesses of 23, 47 and 80 nm on the current collector.

During electrochemical investigations, different behaviors with respect to the Ta_2O_5 film thicknesses have been obtained. Although highest areal capacitance values of $1.94 \mu\text{F cm}^{-2}$ in Emim FSI and $2.84 \mu\text{F cm}^{-2}$ in IG Emim TFSI: PVdF 80:20 are presented for 23 nm films, degradation reactions are found simultaneously when cell voltages higher than 10 V are used. This phenomenon was found to represent the dielectric breakdown of the isolating Ta_2O_5 . 47 and 80 nm thick films, on the other hand, show stable CV cycling at high cell voltages up to 20 V. The same is true even at very high scan rates of 5000 mV s^{-1} .

Additionally, stable cycling was found for 47 and 80 nm thin films in IL as well as IG electrolyte for 2000 cycles at 500 mV s⁻¹. In total, the deposition of 47 nm of Ta₂O₅ displayed most promising results as a good trade-off of areal capacitance, rate capability and cycling stability is achieved. In terms of electrolyte comparison, the IG displays very similar results to the IL, which indicates that this electrolyte can be used to realize all-solid-state prototypes for micro energy storage devices in future works. In order to utilize these promising results most efficiently, improvements of the presented cell concept using 3D dielectric electrode combining 3D silicon scaffold coated with TaN / Ta₂O₅ layers made by Atomic Layer Deposition as well as the realization of the pseudocapacitive electrode with MnO₂ thin film technique will be investigated in the future.

4. Experimental

Sputtering Deposition of TaN and Ta₂O₅ Thin Films: In this work TaN-based (acting as current collector) and Ta₂O₅ (acting as barrier dielectric layer) were deposited as thin films on a [001]-oriented Si substrate using DC sputtering under vacuum method. All depositions were carried out from a Ta target (Neyco -4" diameter -99.95 %) installed in an Alliance Concept CT200 sputtering cluster deposition tool.

Depositing TaN from the Ta target required working in reactive sputtering mode. To achieve the TaN layer the reactive sputtering was set with a mixed plasma composed of N₂ and Ar. The pressure inside deposition chamber as well as the N₂ / Ar + N₂ gas flow ratio were set to ensure a TaN layer with a good conductivity of 640 S cm⁻¹. More details about the deposition parameters can be found in this work [15].

The Ta₂O₅ deposition required working in reactive sputtering mode. To achieve the Ta₂O₅ barrier layer the pressure as well as the O₂ / (Ar + O₂) gas flow ratio were set to obtain high dielectric barrier behaviour. More details about the deposition can be found in this work [15].

X-ray diffraction (XRD) analyses were performed using a Rigaku SmartLab diffractometer in Bragg-Brentano configuration equipped with a Hypix detector, a 9-kW rotating anode, delivering Cu K α radiation ($\lambda = 1.5418 \text{ \AA}$). An offset of 2° relative to the substrate was applied to prevent detector saturation due to the high intensity of the silicon (100) reflection.

X-Ray photoelectron spectroscopy (XPS) analyses were performed with a 5600 Physical Electronics system and collected from a monochromatic K α X-ray source (1486.6 eV) and a spherical energy analyzer. After the subtraction of the Shirley-type background, the core-level spectra were decomposed into their components with mixed Gaussian-Lorentzian shape lines using the Multipack software.

Raman spectra were collected using a LabRAM HR800 Raman spectrometer with an excitation wavelength of 473 nm (HORIBA Scientific, Jobin-Yvon).

Scanning electron microscopy (SEM) images were recorded using a Zeiss Ultra 55 for cross section analyses

X-Ray Reflectometry (XRR) analyses were carried out using the same diffractometer as XRD analyses but in parallel beam mode, and the data was collected from a $\theta/2\theta$ scan ranging from 0 to 10°. XRR scans were afterward with the fitting software Reflex [38]

The MnO₂ counter electrodes have been prepared as oversized and self-standing. MnO₂ (Erachem), carbon black (Super Graphite, Superior Graphite Co.) and PTFE (Sigma Aldrich, 60 % suspension) were combined in a weight ratio of 60:30:10. This mixture was grinded in a mortar with the addition of a few drops of EtOH for 10 min to form a viscous paste, which was subsequently transferred to a glass plate, kneaded, rolled out and folded repeatedly. After the final roll out, electrodes with a diameter of 5 mm ($A = 0.2 \text{ cm}^2$) and a thickness of 0.2 mm were punched out. These electrodes resulted to an average mass loading of 10 mg cm⁻².

The Electrolytes were stored in a glove box (LabMaster, MBRAUN GmbH) under inert argon atmosphere with values of water and oxygen

content below 0.1 ppm. The ionic liquid Emim FSI (Solvionic, 99,99 %) was used neat as is. To form the ionogel, 8 wt% of PVdF (Solef 6008, Solvay) was dissolved in Dimethylformamid (DMF, Sigma Aldrich). Emim FSI with a mass four times higher than the one of PVdF was added to this solution. This mixture was stirred for 15 min. The finished solution was drop casted on to a glass plate and the yielded wet film was dried under vacuum in a tubular oven at 120 °C for 2 h to evaporate the DMF. The dried ionogel film of Emim FSI: PVdF 80:20 was stored in a glove box (LabMaster, MBRAUN GmbH) under inert argon atmosphere with values of water and oxygen content below 0.1 ppm. For utilization, electrolyte circles of IG with a diameter of 6 mm have been cut out, which resulted to a film thickness of 160 μm .

The conductivity was determined by impedance spectroscopy in the frequency range of 10 Hz to 1 MHz using a multichannel potentiostatic-galvanostatic workstation (BioLogic Science Instruments, VMP3 with ECLab software) in the temperature range of -20 to 80 °C.

The conductivity σ was calculated from the measured electrolyte resistance R (intersection with real axes in nyquist plot) via

$$\sigma = \frac{l \times k}{R \times A} \quad (4)$$

where l is the fixed distance between the electrodes in the case of liquid Emim FSI or the thickness of the ionogel Emim FSI: PVdF 80:20. k is a correcting cell factor determined with a standard electrolyte of 0.1 M KCl in H₂O and A is the area of the electrolyte between the electrodes.

The investigated electrochemical cells were assembled in a 2-electrode setup, where the working electrode was the Ta₂O₅ thin film electrode and the counter electrode was the oversized self-standing MnO₂ composite. In the case of Emim FSI as electrolyte, a glass fiber separator (Whatman) was used to separate the two electrodes. A volume of 50 μl of IL was used. In the case of IG as electrolyte, no separator was needed.

Electrochemical tests were performed using a multichannel potentiostatic-galvanostatic workstation (BioLogic Science Instruments, VMP3 with ECLab software) at room temperature.

Cyclic voltammetry (CV) experiments were exerted at a scan rate of 100 to 5000 mV s⁻¹ with a cell voltage of 1 to 20 V. All electrochemical tests have been carried out subsequently for each combination of thin film thickness and electrolyte. Areal capacitances have been calculated by dividing the measured current by the used scan rates and the electrode area of 0.28 cm⁻².

Data availability statement

The data that support the findings of this study are available from the corresponding author upon reasonable request.

CRediT authorship contribution statement

Patrick Gerlach: Conceptualization, Data curation, Formal analysis, Investigation, Methodology, Visualization, Writing – original draft. **Cédric Teyssédou:** Data curation, Formal analysis, Investigation, Methodology, Writing – original draft. **Jérémie Chaillou:** Data curation, Formal analysis. **Isabelle Roch-Jeune:** Data curation, Formal analysis. **Camille Douard:** Writing – review & editing. **Pascal Roussel:** Supervision, Writing – review & editing, Project administration. **Jean Le Bideau:** Funding acquisition, Resources, Supervision, Writing – review & editing. **Christophe Lethien:** Funding acquisition, Project administration, Resources, Supervision, Writing – review & editing. **Thierry Brousse:** Funding acquisition, Project administration, Resources, Supervision, Writing – review & editing.

Declaration of competing interest

The authors declare the following financial interests/personal

relationships which may be considered as potential competing interests:

Prof. Thierry Brousse reports financial support was provided by French Research Agency ANR. If there are other authors, they declare that they have no known competing financial interests or personal relationships that could have appeared to influence the work reported in this paper.

Acknowledgment

This research was funded by the French Research Agency ANR AAPG2022 “MEMPACAP”. The authors thank the French National Research Agency (STORE-EX Labex Project ANR-10-LABX-76–01). The French RENATECH network and the University of Lille are greatly acknowledged for supporting the Center of MicroNanoFabrication (CMNF) facility from IEMN. The authors also want to thank the Chevreur Institute (FR 2638) for funding XRD facility. This work received funding from the CPER Hauts de France project IMTECH and MEL.

Data availability

Data will be made available on request.

References

- [1] H. Liu, et al., Emerging miniaturized energy storage devices for microsystem applications: from design to integration, *Int. J. Extreme Manuf.* (2020), <https://doi.org/10.1088/2631-7990/abba12>.
- [2] K.H. Dinh, et al., Advances on microsupercapacitors: real fast miniaturized devices toward technological dreams for powering embedded electronics? *ACS Omega* (2023) <https://doi.org/10.1021/acsomega.2c07549>.
- [3] B. Jolayemi, et al., Emerging capacitive materials for on-chip electronics energy storage technologies, *Batteries* (2024), <https://doi.org/10.3390/batteries10090317>. (Basel).
- [4] Y. Lu, et al., 3D printed flexible zinc ion micro-batteries with high areal capacity toward practical application, *Adv. Funct. Mater.* (2024).
- [5] P. Li, et al., Rechargeable micro-batteries for wearable and implantable applications, *Small Struct.* (2022).
- [6] N.J. Dudney, Thin film micro-batteries, *Electrochem. Soc. Interface* (2008), <https://doi.org/10.1149/2.F04083IF>.
- [7] T. Schoetz, Disentangling faradaic, pseudocapacitive, and capacitive charge storage: a tutorial for the characterization of batteries, supercapacitors, and hybrid systems, *Electrochim. Acta* (2022).
- [8] A. Burke, Prospects for the development of high energy density dielectric capacitors, *Appl. Sci.* (2021), <https://doi.org/10.3390/app11178063>.
- [9] E. Hourdakis, A.G. Nassiopoulou, Microcapacitors for energy storage: general characteristics and overview of recent progress, *Phys. Status Solidi* (2020), <https://doi.org/10.1002/pssa.201900950> (a).
- [10] Kierzek K. (2020). Activated carbons and their evaluation in electric double layer capacitors.
- [11] K. Brousse, et al., Electrochemical behavior of high performance on-chip porous carbon films for micro-supercapacitors applications in organic electrolytes, *J. Power. Sources* (2016), <https://doi.org/10.1016/j.jpowsour.2016.08.017>.
- [12] T. Brousse, et al., To Be or Not To Be Pseudocapacitive? *J. Electrochem. Soc.* (2015).
- [13] V. Augustyn, et al., Pseudocapacitive oxide materials for high-rate electrochemical energy storage, *Environ. Sci.* (2014).
- [14] C. Lethien, et al., Challenges and prospects of 3D micro-supercapacitors for powering the internet of things, *Energy Environ. Sci.* (2019), <https://doi.org/10.1039/C8EE02029A>.
- [15] C. Teyssedou, et al., Electrolytic micro-capacitors based on tantalum films for high voltage applications, *Adv. Mater. Technol.* (2024).
- [16] E. Atanassova, Thin RF sputtered and thermal Ta2O5 on Si for high density DRAM application, *Microelectron. Reliab.* (1999), [https://doi.org/10.1016/S0026-2714\(99\)00038-4](https://doi.org/10.1016/S0026-2714(99)00038-4).
- [17] S.V.J. Chandra, et al., Effect of substrate temperature on the structural, optical and electrical properties of dc magnetron sputtered tantalum oxide films, *Appl. Surf. Sci.* (2008), <https://doi.org/10.1016/j.apsusc.2007.08.005>.
- [18] M. Pourbaix, *Atlas of Electrochemical Equilibria in Aqueous Solutions* (1966).
- [19] Y. Freeman, *Tantalum and Niobium-Based Capacitors*, Springer, 2020.
- [20] M. Toupin, et al., Charge storage mechanism of MnO₂ electrode used in aqueous electrochemical capacitor, *Chem. Mater.* (2004), <https://doi.org/10.1021/cm049649j>.
- [21] C. Xu, et al., Mesoporous nanowire array architecture of manganese dioxide for electrochemical capacitor applications, *Chem. Commun.* (2009), <https://doi.org/10.1039/b915016a>.
- [22] C. Douard, et al., Electrode design for MnO₂-based aqueous electrochemical capacitors: influence of porosity and mass loading, *Materials* (2021), <https://doi.org/10.3390/ma14112990>. (Basel).
- [23] D.P. Dubal, et al., Effect of different modes of electrodeposition on supercapacitive properties of MnO₂ thin films, *Appl. Surf. Sci.* (2011), <https://doi.org/10.1016/j.apsusc.2010.11.028>.
- [24] B. Babakhani, D.G. Ivey, Effect of electrodeposition conditions on the electrochemical capacitive behavior of synthesized manganese oxide electrodes, *J. Power Sources* (2011), <https://doi.org/10.1016/j.jpowsour.2011.08.102>.
- [25] N.R. Chodankar, et al., Flexible all-solid-state MnO₂ thin films based symmetric supercapacitors, *Electrochim. Acta* (2015), <https://doi.org/10.1016/j.electacta.2015.02.246>.
- [26] T. Guillemin, et al., Solid-state 3D micro-supercapacitors based on ionogel electrolyte: influence of adding lithium and sodium salts to the ionic liquid, *Energy Storage Mater.* (2022), <https://doi.org/10.1016/j.ensm.2022.05.041>.
- [27] A. Ray, B. Saruhan, Application of Ionic Liquids for Batteries and Supercapacitors, *Materials* (2021), <https://doi.org/10.3390/ma14112942>. (Basel).
- [28] E. Pamaté, Binary mixtures of ionic liquids based on EMIm cation and fluorinated anions: physico-chemical characterization in view of their application as low-temperature electrolytes, *J. Mol. Liq.* (2020).
- [29] Yambou, et al., Electrical double-layer capacitors based on a ternary ionic liquid electrolyte operating at low temperature with realistic gravimetric and volumetric energy outputs, *ChemSusChem* (2021).
- [30] G. Kaur, et al., Diverse applications of ionic liquids: a comprehensive review, *J. Mol. Liq.* (2022), <https://doi.org/10.1016/j.molliq.2022.118556>.
- [31] K. Karuppasamy, et al., Ionic liquid-based electrolytes for energy storage devices: a brief review on their limits and applications, *Polymers* (2020), <https://doi.org/10.3390/polym12040918>. (Basel).
- [32] X. Fan, et al., Ionogels: recent advances in design, material properties and emerging biomedical applications, *Chem. Soc. Rev.* (2023), <https://doi.org/10.1039/D2CS00652A>.
- [33] T.K.L. Nguyen, T.N. Pham-Truong, Recent advancements in gel polymer electrolytes for flexible energy storage applications, *Polymers* (2024), <https://doi.org/10.3390/polym16172506>. (Basel).
- [34] C. Xu, et al., Roadmap on ionic liquid electrolytes for energy storage devices, *Chem. Asian J.* (2021), <https://doi.org/10.1002/asia.202001414>.
- [35] M. Stoehr, et al., Raman scattering from epitaxial TaNx (0.94<x<1.37) layers grown on MgO(001), *J. Appl. Phys.* (2007).
- [36] M.T. Brumbach, et al., Evaluating tantalum oxide stoichiometry and oxidation states for optimal memristor performance, *J. Vac. Sci. Technol. A: Vac. Surf. Films* (2014).
- [37] A. Van Der Lee, Grazing incidence specular reflectivity: theory, experiment, and applications, *Solid State Sci.* (2000), [https://doi.org/10.1016/S1293-2558\(00\)00119-9](https://doi.org/10.1016/S1293-2558(00)00119-9).
- [38] G. Vignaud, Gibaud, REFLEX : a program for the analysis of specular X-ray and neutron reflectivity data, *J. Appl. Crystallogr.* (2019).
- [39] T.S. Bhat, et al., Recent trends in electrolytes for supercapacitors, *J. Energy Storage* (2022), <https://doi.org/10.1016/j.est.2022.104222>.
- [40] A.G. Revesz, J.F. Allison, Electronic properties of the silicon-thermally grown tantalum oxide interface, *IEEE Trans. Electron. Devices* (1976), <https://doi.org/10.1109/T-ED.1976.18444>.
- [41] C. Chaneliere, Tantalum pentoxide (Ta2O5) thin films for advanced dielectric applications, *Mater. Sci. Eng. R Rep.* (1998).